Available online at www.sciencedirect.com

SciVerse ScienceDirect

Ceramics International 39 (2013) 2915–2932

CERAMICS INTERNATIONAL

www.elsevier.com/locate/ceramint

Effect of SiC content, additives and process parameters on densification and structure–property relations of pressureless sintered ZrB_2–SiC composites

Manab Mallik[a,b], Sabyasachi Roy[a], K.K. Ray[a], R. Mitra[a,*]

[a]Department of Metallurgical and Materials Engineering, Indian Institute of Technology, Kharagpur-721302, India
[b]Department of Metallurgical and Materials Engineering, National Institute of Technology, Durgapur-713209, India

Received 31 August 2012; accepted 20 September 2012
Available online 29 September 2012

Abstract

The effect of SiC content, additives, and process parameters on densification and structure–property relations of pressureless sintered ZrB_2–(10–40 vol%) SiC particulate composites have been studied. The ZrB_2–SiC composite powders mixed by ball-milling with 1.2 wt% C (added as phenolic resin) and 3 wt% B_4C have been uniaxially cold-compacted and sintered in argon environment at 1950–2050 °C for 2 h, or at 2000 °C for durations between 1/2 and 3 h. The amount of densification is found to increase with sintering duration, and by prior holding at 1250 and 1600 °C for reduction of oxide impurities (ZrO_2, B_2O_3 and SiO_2) on powder particle surfaces by the aforementioned additives. Presence of SiC with average size smaller than that of ZrB_2 appears to aid in densification by enhancing green density, increasing WC content by erosion of milling media, and inhibiting matrix grain growth. Both SiC and WC appear to aid in reduction of oxide impurities. Furthermore, the impurities enriched in W, Fe and Co obtained from milling media are found to be segregated at ZrB_2 grain boundaries, and appear to assist in densification by forming liquid phase, which completely wets the ZrB_2 grains. Hardness increases with SiC content or with sintering duration till 1 h, but decreases for periods ≥ 2 h due to grain growth. The experimentally measured elastic moduli approaches corresponding theoretically predicted values with increasing SiC content due to reduction in porosity.

Keywords: A. Sintering; B. Composites; C. Mechanical properties; D. Borides

1. Introduction

Zirconium diboride (ZrB_2), an ultra high temperature ceramic (UHTC) with melting temperature of 3250 °C is of interest due to high electrical and thermal conductivities as well as moderate density [1–4]. The density of ZrB_2 is lower than that of niobium-based refractory alloys, which requires protection against oxidation and ablation for aerospace applications. With addition of SiC as reinforcement to ZrB_2, its density and thermal expansion coefficients are further reduced, whereas thermal conductivity, oxidation and ablation resistance as well as ability to retain strength at elevated temperature are significantly improved [1,3,5]. This unique combination of properties makes the ZrB_2 based materials attractive for various potential high-temperature thermal and structural applications at temperatures up to 2000 °C [1,2], which include leading-edges in hypersonic re-entry type space vehicles, propulsion systems, furnace heating elements, refractory crucibles, and plasma-arc electrodes [2,5–8].

Processing of the ZrB_2 from powdered raw materials to completely densified form is considered to be difficult, because of the covalent character of its bonding as well as lower magnitudes of both lattice and grain boundary diffusion rates. Therefore, densification of pure ZrB_2 powder generally requires very high temperatures [9] (≥ 2100 °C) with moderate pressure (≈ 20–30 MPa), [10–12] or lower temperatures (~ 1800 °C) with extremely high pressures (> 800 MPa) [13–14]. In recent years, significant attention has been devoted to pressureless sintering of the ZrB_2 and ZrB_2-based composites, as this process is relatively inexpensive compared to hot pressing and offers the flexibility of near-net shaping of the finished products [15–31]. Densification of the pressurelessly sintered ZrB_2 based materials can be more easily

*Corresponding author. Tel.: +91 3222 283292; fax: +91 3222 282280.
E-mail address: rahul@metal.iitkgp.ernet.in (R. Mitra).

0272-8842/$ - see front matter © 2012 Elsevier Ltd and Techna Group S.r.l. All rights reserved.
http://dx.doi.org/10.1016/j.ceramint.2012.09.066

achieved by addition of SiC, B_4C, TiC or AlN in the form of reinforcement or additive, as has been reported by Kida and Segawa [15–16] Recently, Silvestoni et al. [17] and Sciti et al. [18] have reported about the densification of ZrB_2 and HfB_2 based composites by pressureless sintering with addition of $MoSi_2$, which enhances the process of densification through formation of a borosilicate liquid film at matrix grain boundaries and particle–matrix interfaces. However, formation of such a film with low melting temperature at grain boundaries or interfaces is not desirable for elevated temperature applications.

In contrast to the liquid phase formers, reactive agents such as B_4C, C, WC and VC combined with control of the sintering atmosphere, can be used to promote densification through solid state sintering by removal of surface oxides (ZrO_2 and B_2O_3 for ZrB_2) [19–30]. In some of the reports [20–24,29,30], it has been shown that it is possible to achieve relative density of $\geq 98\%$ through pressureless sintering of ZrB_2 or ZrB_2–SiC composites using B_4C and C as additives. Furthermore, Zhang et al. [24] have demonstrated that it is possible to attain relative densities and mechanical properties comparable to those in the hot-pressed ZrB_2 based composites by carrying out pressureless sintering of ZrB_2 with 10–30 vol% SiC reinforcement using B_4C and phenolic resin as additives. Although WC has been reported to contribute to the process of densification of ZrB_2 and ZrB_2–SiC composites [19,20,26,27], the mechanisms proposed by the different investigators appear to be quite varied. It has been shown that WC is relatively less effective in reduction of surface oxides than B_4C and C [20] or VC in case of ZrB_2 [26]. Furthermore, WC has been reported to aid in the process of densification by forming solid solutions with ZrB_2 [19,27,28]. In addition, W formed through the reduction of ZrO_2 by WC has been found to react further with SiC and form WSi_2, which in turn contributes to sintering at 2200 °C by formation of liquid phase [27]. Besides densification, oxidation resistance of ZrB_2 has been reported to improve significantly by addition of 4 mol% WC, as formation of WO_3 promotes liquid phase sintering of the oxide scale [28].

Based on preliminary studies by Mallik et al. [30], it has been reported that the ZrB_2–SiC composites with higher reinforcement content show greater densification, indicating that besides the sintering additives, the SiC particles could have a role as well, which needs to be fully understood. The effect of SiC volume fraction on densification behavior needs to be examined synergistically with that of additives and impurities with due emphasis on understanding of the operative mechanisms. Moreover, there is need to arrive at optimum temperature and duration of sintering, so as to obtain desired combination of relative density, microstructure and mechanical properties. Therefore, the present report is focused on studies comprising pressureless sintering of the ZrB_2–(10–40 vol%) SiC composites at 2000 °C for time-periods ranging from 1/2 to 3 h in order to examine the effects of temperature and duration of sintering, holding at intermediate temperatures as well as SiC content on their densification, matrix grain size, and mechanical properties.

2. Experimental procedure

2.1. Preparation of composites

Commercially available powders of ZrB_2, α-SiC (6H) and B_4C, each with 99.5% purity were used as raw materials in this study. Powders of ZrB_2 and SiC were obtained from the H.C. Starck, GmbH, Goslar, Germany, whereas the B_4C powder was purchased from the Boron Carbide India Limited, Mumbai, India. Furthermore, phenolic resin (phenol formaldehyde with ethanol as solvent), type ABRON PR100 obtained from ABR Organics Limited, Hyderabad, India, has been used as source of carbon in the raw materials. The carbon content of the phenolic resin has been found to be ≈ 37 wt% by thermogravimetric analysis. For ZrB_2, a powder sample (ZBC) having compositions of $ZrB_2 + 5.6$ vol% (3 wt%) $B_4C + 10.1$ vol% (3.2 wt%) phenolic resin was prepared, such that the carbon content was 3.3 vol% (1.2 wt%) C. Additional powder samples having the compositions of ZBC-10 vol% SiC (ZSBC-10), ZBC-20 vol% SiC (ZSBC-20), ZBC-30 vol% SiC (ZSBC-30), and ZBC-40 vol% SiC (ZSBC-40) were also prepared. These samples were mixed using a planetary mono-mill (model Pulverisette 6, Fritsch GmbH, Idar-Oberstein, Germany) operated at 250 rpm for 6 h. The mixing was carried out using ethanol as the medium inside WC–Co vials with the help of balls made of the same material. After the completion of milling, ethanol was drained out, and the blended powders were dried at 350 °C for 2 h in air. The composite powders were next crushed using agate mortar and pestle, and were uniaxially pressed at 100 MPa inside a steel die with 25 mm diameter to form pellets with 5.2–5.4 mm height.

The green compacts were heated to 850 °C at the rate of 10 °C/min, held there for 1 h, and were then sintered at 2000 °C in a high-temperature ASTRO furnace (Thermal Technology LLC, Santa Rosa, California, USA)) having graphite heating element for time duration of 1/2, 1, 2 or 3 h in flowing argon. The intermediate hold at 850 °C was carried out in order to ensure suitable conversion of resin to carbon along with loss of volatile products. Some of the samples were held for 1/2 h at intermediate temperatures of both 1250 and 1600 °C, following which sintering was carried out at 2000 °C. After sintering, the furnace was allowed to cool to room temperature at the rate of 10 °C/min with the samples exposed to flowing argon. For the purpose of optimizing the processing temperature, some of the ZSBC-20 samples were also sintered for 2 h either at 1950 or 2050 °C, after prior holding at 850 °C.

2.2. Characterization

2.2.1. Characterization of raw materials

The raw materials were characterized by X-ray diffraction (XRD) using Co K_α radiation to confirm the presence of expected phases. The oxygen contents of these powders were analyzed using an inert gas fusion analyzer (Model TC 400, LECO Corporation, St. Joseph, Michigan, USA).

Moreover, morphology, size and bulk composition of the powders were examined on a JEOL JSM5800 scanning electron microscope equipped with energy dispersive X-ray (EDX) analyzer (Oxford Instruments, Tubney Woods, Abingdon, Oxfordshire, UK).

2.2.2. Characterization of composites

The bulk density of each of the sintered samples was evaluated by Archimedes principle. Relative densities were calculated by normalizing the measured bulk density by the corresponding theoretical density calculated using the rule of mixtures (ROM). The sintered samples were sectioned using an Isomet slow speed precision cutting diamond saw (Buehler Ltd, Lake Bluff, Illinois, USA). The sectioned samples were initially polished sequentially on coarse and fine diamond-coated discs, subsequently on abrasive SiC papers down to 600 grit, and finally on clothes smeared with 6, 1 and 0.25 μm diamond lapping paste. The different phases in the microstructures were also identified by XRD analysis using Co K_α radiation. The microstructures of these composites were examined by field emission scanning electron microscopy (FESEM, SUPRA 40, Carl Zeiss SMT GmbH, Oberkochen, Germany) using both secondary electron (SE) and backscattered electron (BSE) imaging, whereas their chemical compositions were determined using energy dispersive X-ray (EDX) analyses. The specimens for transmission electron microscope (TEM) studies were prepared using routine methods involving successive steps of grinding, polishing, dimpling, and ion-milling. Subsequently, the microstructure of the specimens were examined on a JEM 2100 (JEOL, Tokyo, Japan) TEM operated at an acceleration voltage of 200 kV to observe primarily the grain boundaries and particle–matrix interfaces. Images were recorded using both bright field and dark field TEM modes, while EDX analyses were carried out in order to identify the constituent phases. The average sizes of ZrB_2 grains and SiC particles were obtained from measurements on more than 100 grains or particles for each of these phases by subjecting the SEM micrographs depicting the microstructures to image analysis using the BIOVIS software.

2.2.3. Elastic modulus measurement

Circular disc-shaped specimens with dimensions of 20 mm diameter and 4 mm thickness were used to measure the elastic moduli using the ultrasonic technique (Model Epoch 4, Panametrics-NDT, Wattham, MA, USA). These tests were performed by measuring the time to send and receive longitudinal and transverse waves in the samples. The Poisson's ratio (ν), Young's modulus (E), shear modulus (G), and bulk modulus (B) were calculated using the expressions:

$$v = \frac{1-2(V_T/V_L)^2}{2-2(V_T/V_L)^2} \quad (1)$$

$$E = \frac{V_L^2\rho(1+v)(1-2v)}{(1-v)} \quad (2)$$

$$G = V_T^2\rho \quad (3)$$

$$B = \frac{EG}{3(3G-E)} \quad (4)$$

where ρ is the density, and V_L as well as V_T are longitudinal and transverse sound wave velocities, respectively.

2.2.4. Hardness and fracture toughness measurement

The Vickers microhardness was measured at the ambient temperature (298 K) using a microhardness tester (Model Micromet 5103, Buehler Inc., Lake Bluff, Illinois, USA) operated using a load of 500 gf for 15 s. Furthermore, for measurement of indentation fracture toughness (IFT), K_C, the polished surfaces of the differently sintered specimens were indented using a Vickers hardness tester (Model LV 700, LECO Corporation, St. Joseph, Michigan, USA) operated at the load of 20 kgf for 15 s. The diagonals of the indentations and lengths of cracks formed at the indentation corners were measured with the help of an optical microscope using the image analysis software. Ten indents were made on each specimen to evaluate the average magnitude of IFT, which was calculated using the following relations [31]:

$$K_{IC} = 0.0123E^{0.4}H^{0.1}\left(\frac{P}{l}\right)^{1/2} \text{ Palmqvist crack model} \quad (5)$$

$$K_{IC} = 0.0309\left(\frac{E}{H}\right)^{0.4}\left(\frac{P}{c^{3/2}}\right) \text{ Median crack model} \quad (6)$$

where E is the Young's modulus (GPa), H is the hardness (GPa), P is the indentation load (N), and c is the characteristic crack length. The value of $c=l+a$, where l is the length of the crack at the indentation corner, and a is half the length of diagonal of an indentation. It may be noted that the Palmqvist model is used when c/a ratio is <3, whereas the median model is useful for c/a ratio ≥ 3.

3. Results

3.1. Characterization of raw materials

The presence of ZrB_2, SiC and B_4C, each having hexagonal crystal structure, in the as-received powders has been confirmed using XRD analyses. The SEM images depicting the powder particles of ZrB_2, SiC and B_4C are shown in Fig. 1(a) through (c), respectively. These images exhibit the particles to be irregularly shaped. The oxygen content and particle size for each type of powder are listed in Table 1. It may be noted that each of the raw materials as shown in this table has significant oxygen content, which is expected to be present as oxide impurities on powder particle surfaces.

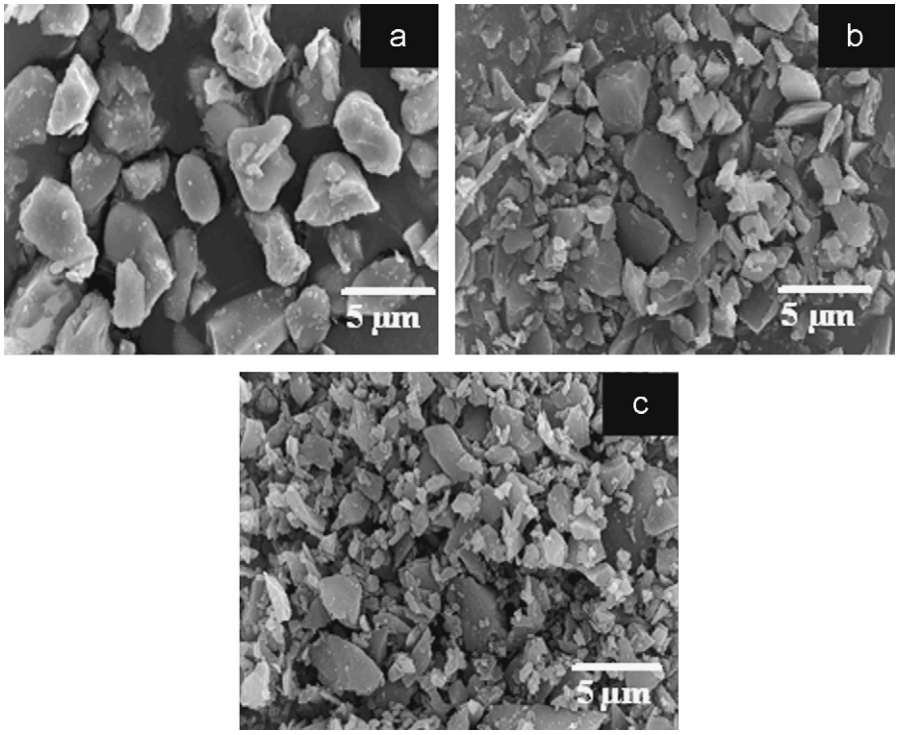

Fig. 1. SEM images depicting powder particles of: (a) ZrB_2, (b) SiC, and (c) B_4C, which were used as raw materials.

Table 1
Particle size and oxygen content of as-received powders used as raw materials for processing of the investigated ZrB_2–SiC composites.

Powder	Oxygen content (wt%)	Particle size (μm)
ZrB_2	1.3 ± 0.1	3.54 ± 1.2
SiC	0.55 ± 0.01	2.10 ± 0.9
B_4C	1.8 ± 0.2	1.85 ± 0.7

The XRD patterns of the powder mixtures processed by ball-milling, as depicted in Fig. 2, show the peaks of WC in addition to those of the aforementioned raw materials. In contrast, not a single WC peak could be identified in the XRD pattern representing the as-received raw materials. Moreover, the results in Fig. 2 show the peak height of WC to rise with increase in the volume fraction of SiC in the powder mixture. Based on these observations, it is appropriate to attribute the presence of WC in the ball-milled composite powder mixtures to wear and tear of balls and vial made of WC–Co composite by the abrasive SiC particles.

3.2. Green and sintered densities

The green densities of the uniaxially pressed composite pellets have been found to vary from 2.5 to 2.7 g/cc. These values have been compared with the corresponding theoretical densities of the compacts calculated using rule of mixtures (ROM) by considering the theoretical densities of

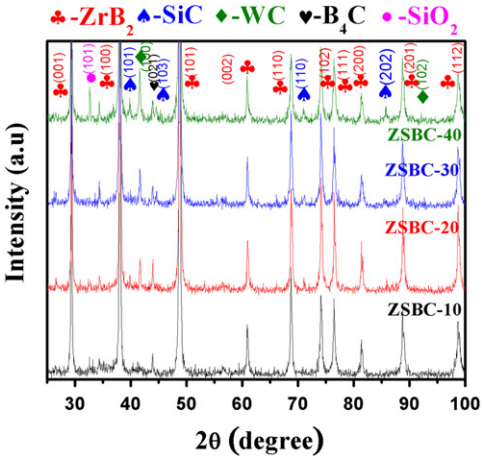

Fig. 2. XRD patterns obtained from the ball-milled composite powders.

ZrB_2 (6.09 g/cm^3), SiC (3.21 g/cm^3), B_4C (2.52 g/cm^3) and phenolic resin (1.14 g/cm^3). The plots depicting the variation of volume shrinkage with SiC volume fraction [Fig. 3(a)], and that of green density against volume shrinkage [Fig. 3(b)] show that (i) the volume shrinkage decreases with increase in SiC volume fraction; and (ii) the relative densities of the green compacts increase with increase in SiC volume fraction.

The sintered products have been found to have diameters between 19 and 20 mm, and heights in the range of 4.0–4.3 mm, which on comparison with the dimensions of the green compacts (as mentioned in Section 2.1) indicates

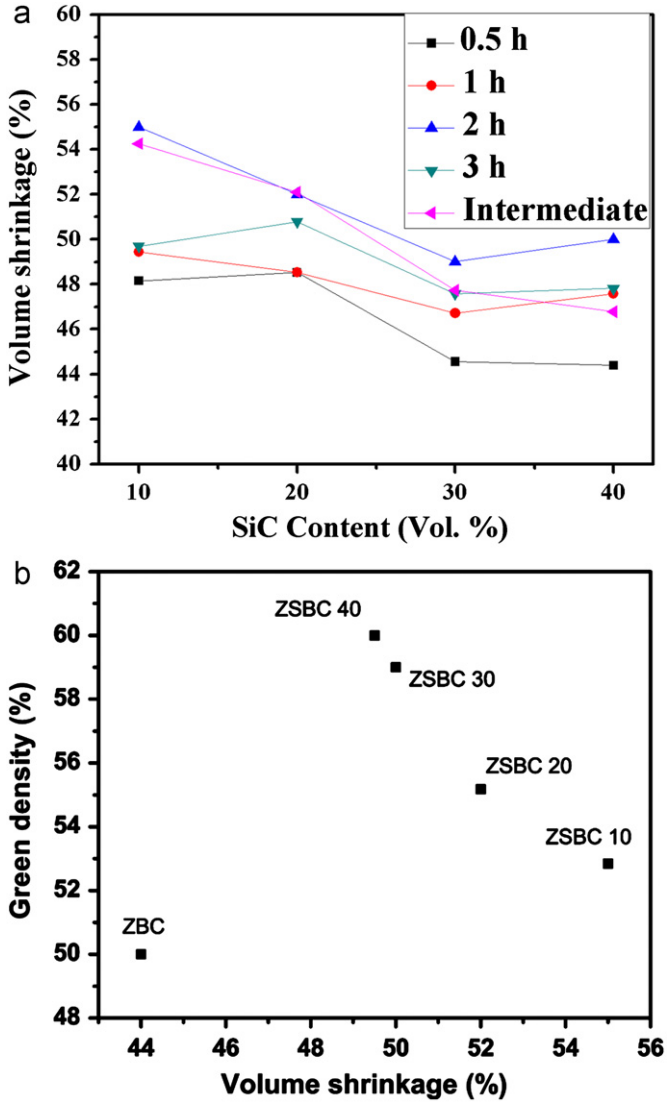

Fig. 3. Plots depicting variation of: (a) volume shrinkage with SiC volume fraction; and (b) green density against volume shrinkage, for sintering carried out at 2000 °C for 2 h.

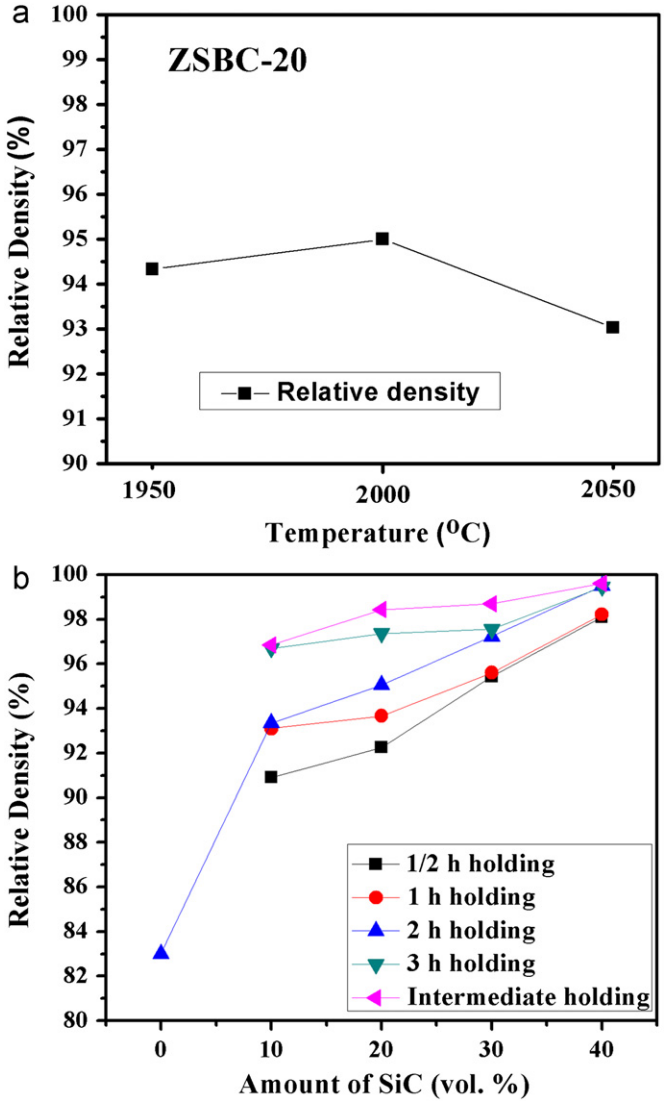

Fig. 4. Plots depicting variations of relative density of the sintered composites: (a) as function of the sintering temperature for the ZSBC-20 composite and (b) as function of the SiC volume fraction.

linear shrinkage in the range of 20–24%. The variations of relative density of the sintered products as function of the sintering temperature for the ZSBC-20 composite and as a function of the SiC volume fraction for all the investigated sintered composites are shown in Fig. 4(a) and (b), respectively. Analyses of the results in Fig. 4(a) indicate that the optimum temperature for achieving maximum relative density by pressureless sintering is 2000 °C, while the values of relative densities of the composites sintered at 1950 or 2050 °C have been found to be less. It may be noted that in a previous report by Zhang et al. [20], the relative density of ZrB_2-4 wt% B_4C has been found to be lowered with increase in the sintering temperature from 2000 to 2050 °C or decrease to 1900 °C, However, the results of an earlier study on ZrB_2-(10–30 vol%) SiC composites with 2.8, 5.0 or 7.3 wt% C have not shown a definite manner of variation [24]. Probably, the amount of additives, initial particle size distribution and green density may also have a strong effect on the temperature required for optimum densification.

From the results shown in Fig. 4(b), the relative densities of the ZrB_2–SiC composites are found to be $>90\%$ of the corresponding theoretical densities calculated from the rule of mixtures, while that of the ZBC is only $\approx 83\%$. Moreover, the values of relative densities are found to increase steadily with increase in volume fraction of SiC. These observations suggest that processing of completely dense pure ZrB_2 is very difficult, while the presence of SiC as reinforcement is significantly beneficial for promoting the process of densification. From comparison of the plots shown in Fig. 4(b), it is also inferred that the extent of densification is increased significantly with increase in the duration of sintering for a composite, for time span between 1/2 and 3 h. This observation is more or less

similar to that reported for ZrB_2 by Chamberlain et al. [19]. In this study, maximum relative density of 99.5% has been achieved in the ZSBC-40 composite, which was sintered for 2 h after holding for 1/2 h at intermediate temperatures of both 1250 and 1600 °C. The values of relative densities obtained in this study are comparable to those of the pressure-less sintered ZrB_2–SiC composites, reported in previous studies [22,24].

3.3. Microstructure

Typical XRD patterns depicting the peaks of the constituent phases in the microstructures of ZBC, ZSBC-10, ZSBC-20, ZSBC-30 and ZSBC-40 composites sintered at 2000 °C for 2 h are shown in Fig. 5. The peaks of B_4C used as sintering additive are also observed in the recorded XRD patterns in this figure. However, unlike the XRD patterns obtained from the ball-milled powder samples, the peaks of WC are not observed in Fig. 5, which is suggestive of either decomposition or chemical reactions involving this phase.

The results of bulk EDX analysis on the investigated composite samples have shown distinct evidence for the presence of W, Co and Fe as impurities in the sintered composites. The atomic fraction of W has been found to be 0.52%, 0.91%, 1.24% and 3.38%, respectively, which indicates that the bulk concentration of this impurity element is increased with increase in SiC content of the investigated composites. This observation is also consistent with increase in the height of the XRD peaks of WC with increase in SiC content of the composite powder mixtures prior to sintering, as shown in Fig. 2 and discussed in Section 3.1. The locations enriched in the aforementioned impurities within the microstructures of the sintered composites have been further investigated using SEM accompanied by EDX mapping, and the results are discussed later in this section.

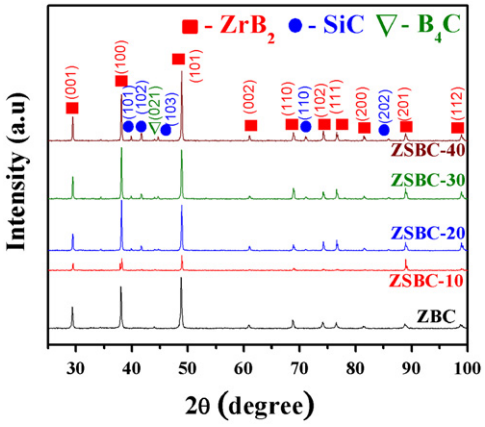

Fig. 5. Typical XRD patterns from ZBC, ZSBC-10, ZSBC-20, ZSBC-30 and ZSBC-40 composites sintered at 2000 °C for 2 h.

The microstructures of the ZSBC-40 composite sintered at 2000 °C for 1/2 and 1 h are shown in Fig. 6(a) and (b), respectively. Furthermore, the SEM (BSE) images depicting the microstructures of ZBC, ZSBC-10, ZSBC-20, ZSBC-30 and ZSBC-40 composites sintered at 2000 °C for 2 h are shown in Fig. 7(a) through (e), respectively. As expected, the contrast of different phases or locations in these SEM (BSE) images is found to depend on the average atomic numbers of the constituent elements. While the SiC particles in either ZSBC-10 or ZSBC-20 composite are found to be isolated from one another, this phase appears to be more or less interconnected in both ZSBC-30 and ZSBC-40 composites. The identities of the major elements in each of these constituent phases have been confirmed by EDX analysis.

The microstructures and interfaces of all the investigated composites have been also examined at higher magnification using SEM (BSE) imaging with EDX analysis, and the results are shown in Fig. 8. The SEM (BSE) images in this figure show the presence of an interfacial layer appearing relatively brighter than the ZrB_2 grains and forming a near-continuous network surrounding both matrix grain boundaries and particle–matrix interfaces. The results of EDX mapping as shown in Fig. 8((c)–(g)), indicate the enrichment of impurity elements including W, Fe and Co in this interfacial layer.

An SEM (BSE) image depicting the presence of W-rich phase at ZrB_2-grain boundary and ZrB_2–SiC interface is shown in Fig. 9(a), whereas EDX spectra from the interfacial location and ZrB_2 grain are shown in Fig. 9(b) and (c), respectively. The results of EDX point analysis at the interfacial location [Fig. 9(b)] show a peak of C in

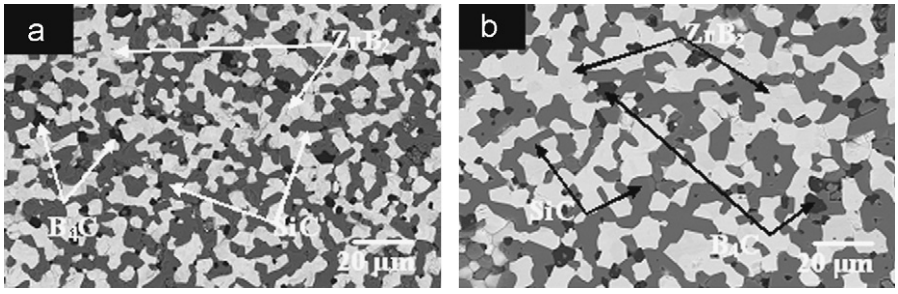

Fig. 6. SEM (BSE) images depicting the microstructures of the ZSBC-40 composite sintered at 2000 °C for: (a) 1/2and (b) 1 h.

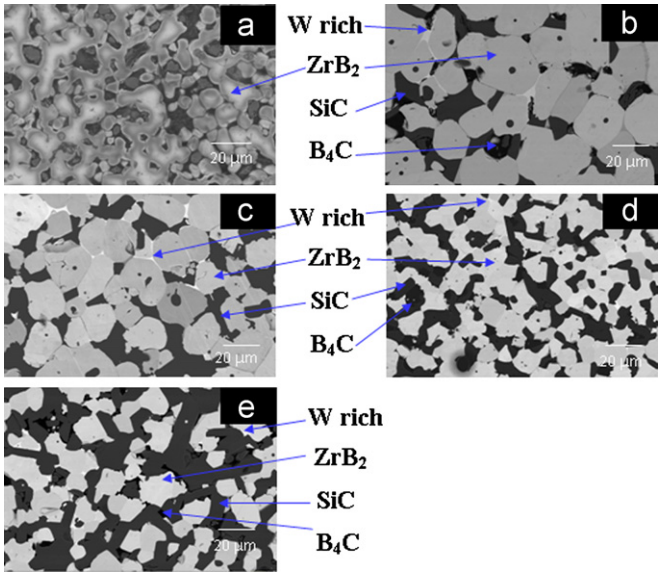

Fig. 7. SEM (BSE) images depicting the microstructures of: (a) ZBC, (b) ZSBC-10, (c) ZSBC-20, (d) ZSBC-30 and (e) ZSBC-40, obtained after sintering at 2000 °C for 2 h.

addition to those of W, Co, and Fe. This observation suggests that a small amount of WC or W_2C could be present at the interfaces, and absence of their peaks in the XRD patterns is probably because their volume fraction is insignificant. Furthermore, it is interesting to note that the EDX spectrum [Fig. 9(c)] from a point within the ZrB_2 grain shows a peak of C in addition to those of Zr and B. This observation suggests that C is probably present forming solid solution, as has been reported in some of the earlier studies [19,22]. The locations appearing darker than SiC in Fig. 9(a) have been identified as either B_4C or C through EDX analyses.

Qualitative comparison of the microstructures shown in Fig. 6(a) with Fig. 6(b) or Fig. 7(e) confirms that the matrix grain size increases with increase in the time of sintering. The plots depicting the variation of grain size with duration of sintering for each of the investigated composites, along with best-fit lines drawn through linear regression analyses are shown in Fig. 10. Moreover, the values of R^2 (between 0.97 and 0.99), slopes, and intercepts estimated from linear regression analyses of the plots in this figure are listed in Table 2. Besides the ZrB_2 grains, the SiC particles appear to have grown in size during sintering so as to develop an aspect ratio varying between 3:1 and 4:1. From the average areas of the SiC particles, their approximate mean sizes have been estimated as 10.2 ± 3, 10.5 ± 3, 13.7 ± 4, and 15.7 ± 4 for ZSBC-10, ZSBC-20, ZSBC-30 and ZSBC-40, respectively

Quantitative image analyses of the SEM micrographs depicting microstructures of the samples sintered for 2 h at 1950 and 2050 °C, as depicted in Fig. 11(a) and (b), respectively have shown the average matrix grain sizes in the ZSBC-20 to be 8.3 ± 1.6 and 29.3 ± 6.4 μm, respectively. Comparison of these results with those shown in Fig. 8 indicates that sintering at 2000 °C leads to matrix grain size (20.6 ± 5) lying in between these two values. This observation confirms that significant grain growth occurs in these composites with increase in the temperature of sintering.

The study of microstructures using TEM has been focused primarily on examination of matrix grain boundaries and particle–matrix interfaces in the composites. Typical bright field TEM images depicting ZrB_2 matrix grain boundary and ZrB_2–SiC interface are shown in Fig. 12(a) and (b), respectively. Furthermore, the selected area electron diffraction patterns along with EDX spectra from ZrB_2 and SiC as depicted in Fig. 12(b), are shown in Fig. 12(c) and (d), respectively. The TEM studies have also confirmed the presence of microporosities at the grain boundary triple points within the ZrB_2 matrix, as shown in Fig. 12(a). Moreover, a phase found to be present at the ZrB_2–SiC interface, as shown in Fig. 12(b) has been found to be enriched in W and Fe by EDX analysis.

3.4. Mechanical properties

3.4.1. Microhardness and indentation fracture toughness

Bar charts depicting the microhardness of the investigated composites with different amounts of SiC particles are shown in Fig. 13. Examination of the results in this figure indicates that the microhardness scales with the SiC content of the investigated composites, as expected. The range of experimentally determined microhardness values as shown in Fig. 13 agrees well with those reported earlier in the published literature [32,33]. Examination of the results in this figure leads to the following inferences: (i) the increase in microhardness values is noticeable as the duration of sintering is increased from 1/2 to 1 h; (ii) the value of microhardness either increases or decreases marginally, or remains more or less same for sintering periods between 1 and 2 h and (iii) sintering for beyond an optimum duration of ≈ 2 h causes decrease in hardness; but (iv) for the composites subjected to pre-sintering for 1/2 h at 1250 °C and 1600 °C, the microhardness found after 2 h of sintering is distinctly higher than those heated directly to 2000 °C and sintered at this temperature for 1/2, 1 or 2 h.

The average values of microhardness obtained for the ZSBC-20 composite sintered for 2 h at 1950 and 2050 °C are 1251 ± 43 Hv and 1075 ± 43 Hv, respectively, both of which are significantly lower than the value recorded for the composite sintered for same duration at 2000 °C (1523 ± 45). These results suggest that the microhardness values scale with the amount of densification, besides the SiC content, and therefore it is appropriate to infer that the optimum temperature for sintering in the present study is 2000 °C.

Like microhardness, the indentation fracture toughness (IFT) too is found to increase with SiC volume fraction, as shown by the nature of plot depicted in Fig. 14(a). The paths of cracks at the corners of indentations have been

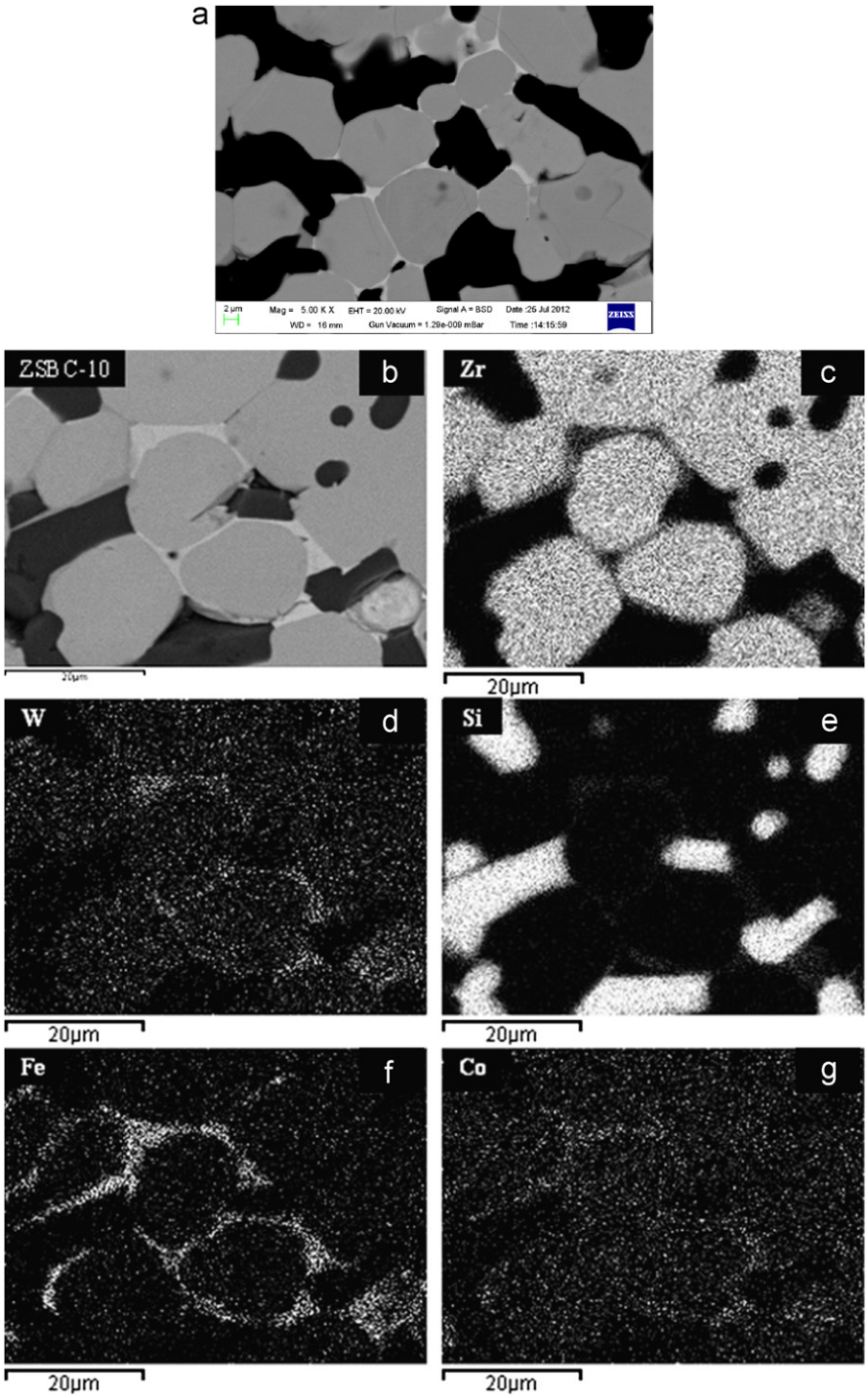

Fig. 8. SEM (BSE) images showing matrix grain boundaries and ZrB_2–SiC interfaces in: (a) ZSBC-40 composite, (b) ZSBC-10 composite at different magnifications; as well as EDX images depicting locations enriched in: (c) Zr, (d) W, (e) Si, (f) Fe, and (g) Co.

examined to identify the toughening mechanisms in the investigated composites. It has been observed that interaction of indentation cracks with the SiC particles as shown in Fig. 14(b), leads to crack deflection, branching and bridging, which in turn are known to cause toughening of the investigated composites.

3.4.2. *Elastic properties*

The Poisson's ratios of the investigated composites have been found to be in the range of 0.12–0.15, estimated using the procedure discussed in Section 2.2.2. These values are within the range of the data reported for this type of ceramic materials. Bar charts depicting the measured

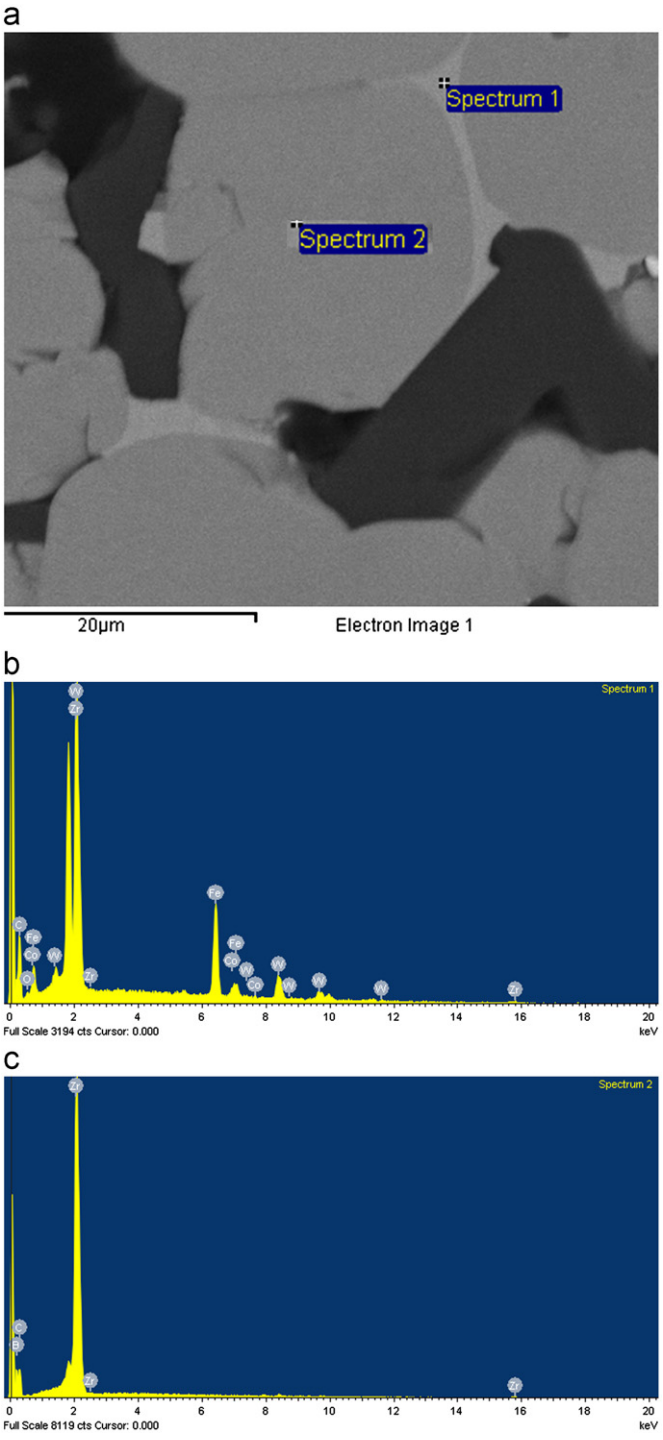

Fig. 9. (a) Typical SEM (BSE) image depicting matrix grain boundary and particle–matrix interface at high magnification, as well as EDX spectrum from: (b) ZrB_2 grain boundary, and (c) ZrB_2 grain.

values of Young's modulus (E), shear modulus (G) and bulk modulus (B) of the pressureless sintered ZrB_2–SiC composites with varying amounts of SiC content are shown in Fig. 15(a)–(c), respectively. In these figures, the bar-charts depicting the values of E, G and B calculated using the ROM by considering the previously reported elastic properties of ZrB_2 ($\approx$500 GPa) [34] and SiC

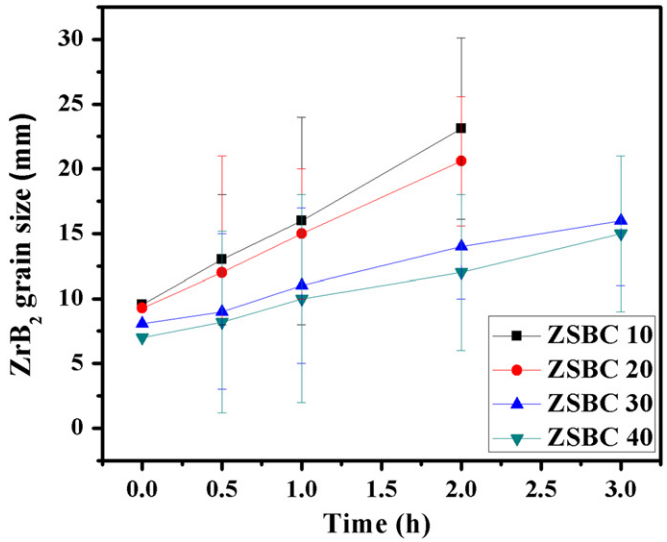

Fig. 10. Plots showing the variation of ZrB_2 grain size as function of sintering time for the ZSBC-10, ZSBC-20, ZSBC-30 and ZSBC-40 composites, sintered at 2000 °C for 2 h. The best-fit lines drawn using linear regressional analyses are also shown.

Table 2
Parameters estimated from linear regressional analyses for the variation of ZrB_2 grain size with duration of sintering for ZSBC-10, ZSBC 20, ZSBC-30 and ZSBC-40 composites.

Composites	ZSBC-10	ZSBC-20	ZSBC-30	ZSBC-40
R^2	0.998	0.999	0.967	0.988
Slope	6.73	5.67	2.76	2.64
Intercept	9.56	9.28	8.08	6.98

($\approx$475 GPa) [35] are also shown for the purpose of comparison.

4. Discussion

4.1. Densification and evolution of microstructure

4.1.1. Effect of SiC reinforcement on compaction and shrinkage during sintering

It has been observed that the presence of SiC particles tends to restrict shrinkage of the ZrB_2 matrix, and as a result, the amount of volume shrinkage decreases with increase in the SiC volume fraction [Fig. 3(a)]. This effect of reinforcement on shrinkage of a given composite during sintering has been theoretically predicted and also experimentally observed by Edrees et al. [36]. It is interesting to note that greater densification is achieved in spite of lower shrinkage in case of the composites with higher SiC volume fraction [Fig. 3(a)]. This observation could be attributed probably to increase in green density of the cold compacted composites with increasing amount of SiC particles, as shown in Fig. 3(b). It is intuitive that higher green density of the compacts results in decrease in

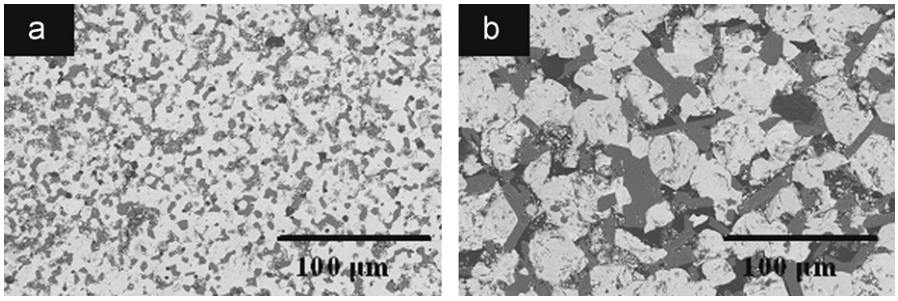

Fig. 11. SEM (BSE) images depicting the microstructures of the ZSBC-20 composite sintered for 2 h at: (a) 1950 and (b) 2050 °C.

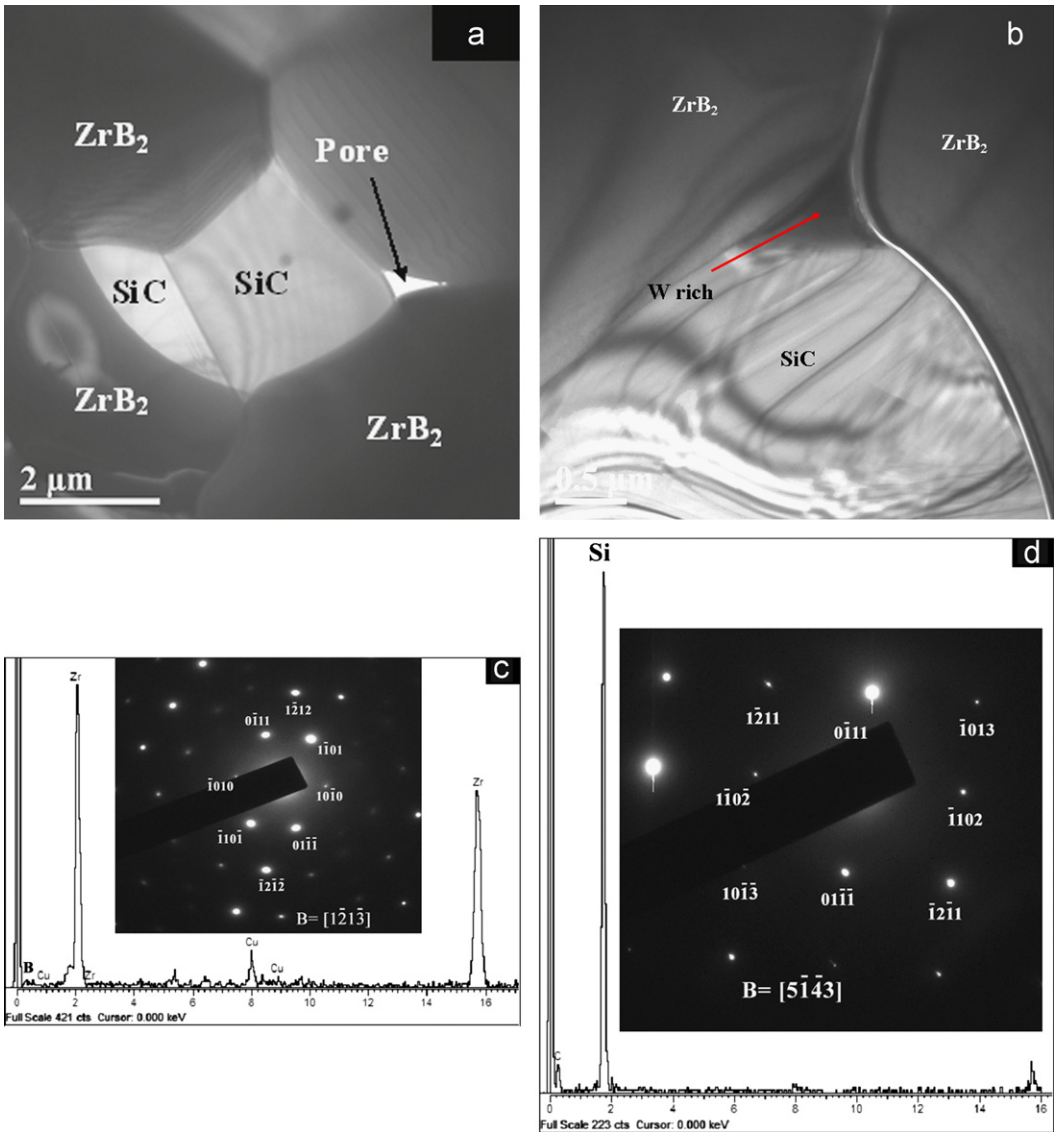

Fig. 12. Bright field TEM images of the ZSBC-20 composite depicting: (a) ZrB_2 grain boundaries, and (b) ZrB_2–SiC interfaces; as well as selected area electron diffraction patterns from: (c) ZrB_2 and (d) SiC. The diffraction patterns are shown as superimposed on EDX spectrum taken from the same location.

diffusion distances between the adjacent particles, which in turn enhances the sinterability of the compacts.

The increase in green density being observed with increase in the volume fraction of SiC particles is attributed to their finer average size than that of ZrB_2 particles, which is expected to lead to much greater packing density through cold compaction. In this context, it may be mentioned that an earlier study involving hot pressing of ZrB_2-30 vol% SiC

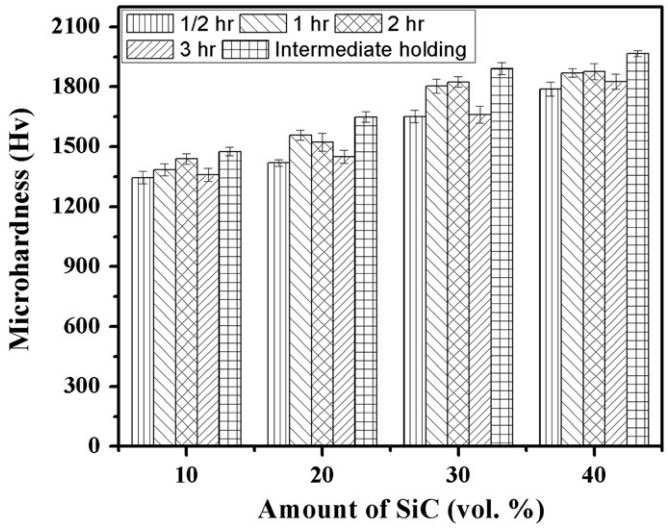

Fig. 13. Bar charts showing microhardness of the pressureless sintered ZrB_2–SiC composites.

composites [37] have shown maximum densification for the finest size of SiC particles.

4.1.2. Effect of additives and SiC on reduction of surface oxides

Addition of B_4C and carbon (left behind after vaporization of phenolic resin) is known to aid in the process of densification by reduction of the surface oxides [21,23]. The temperatures used for pre-sintering at intermediate temperatures of 1250 and 1600 °C were chosen through thermodynamic analyses of the following reduction reactions involving B_4C and C:

$$B_4C(s)+7ZrO_2(s)\rightarrow 7ZrB_2(s)+5CO\ (g)+3B_2O_3(l) \quad (7)$$

$$B_2O_3\ (l)+ZrO_2\ (s)+5C\ (s)\rightarrow ZrB_2\ (s)+5CO\ (g) \quad (8)$$

$$B_2O_3\ (l)+7C\ (s)\rightarrow B_4C\ (s)+6CO\ (g) \quad (9)$$

$$SiO_2\ (s)+3C\ (s)\rightarrow SiC\ (s)+2CO\ (g) \quad (10)$$

$$SiC\ (s)+6B_2O_3\ (l)\rightarrow 7SiO_2\ (s)+3B_4C\ (s)+4CO\ (g) \quad (11)$$

In this study, the aforementioned reactions (7–11) have been found to cause weight loss in the range of 9–14 wt% during the process of sintering due to the loss of volatile reaction products. However, no definite trend has been observed in the variation of weight loss with either SiC content or temperature of sintering.

Reaction (7) has been first proposed by Zhang et al. [20], whereas reaction (8) has been suggested earlier by Zhu et al. [22]. Furthermore, through a more comprehensive study, reactions (7–10) have been suggested by Zhang et al. [24]. In addition, it has been shown by Zhu et al. [21] that combination of B_4C and C additions is more effective in removal of surface oxides than these additives alone, as both ZrO_2 and B_2O_3 are removed simultaneously. It has been shown that B_2O_3 present in the powders used as raw materials and also formed by reaction (7), reacts with the

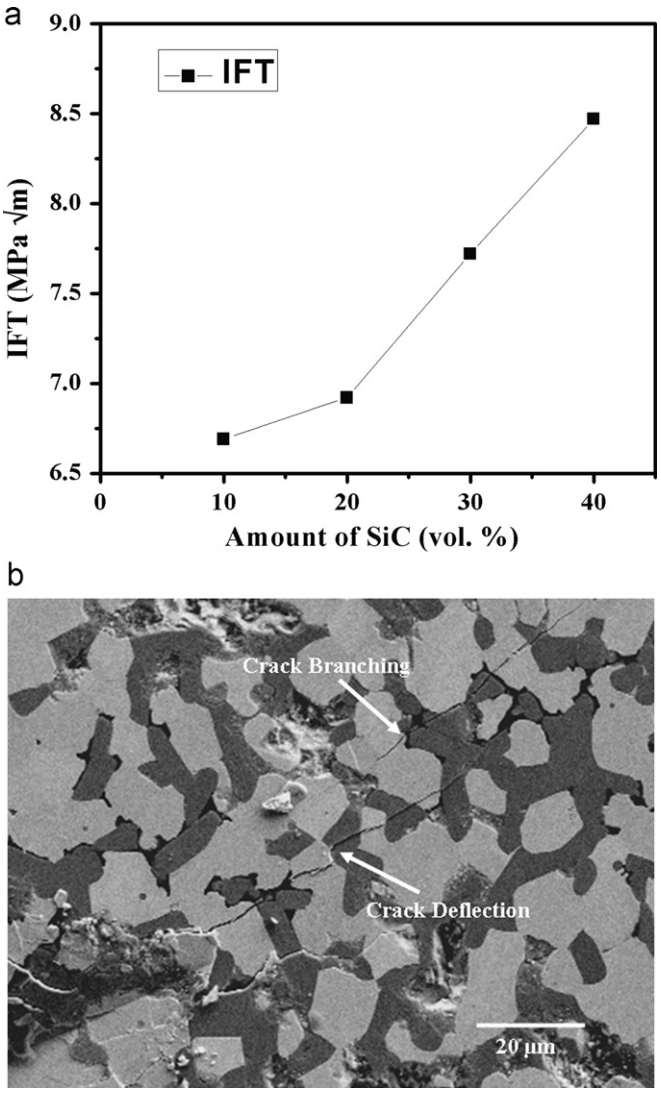

Fig. 14. (a) Plot showing the variation of indentation fracture toughness (IFT) with SiC content of the investigated composites; and (b) SEM image showing Vickers indentation on the ZSBC-30 composite, and the propagation of indentation crack revealing crack deflection, branching and bridging.

SiO_2 present in the SiC powders to form borosilicate glass, which in turn promotes coarsening of the ZrB_2 grains, and thereby the process of densification remains incomplete [24,38]. By addition of C, the intergranular B_2O_3 can be reduced through Reaction (8), and thereby densification can be promoted. Therefore, the amount of densification in a given ZrB_2–SiC composite has been found to depend on whether sufficient carbon is added in proportion to the net oxygen content of the raw materials [24].

Plots of free energy change against absolute temperature using thermodynamic data [39] for reactants and products in the aforementioned reactions are shown in Fig. 16, from which it is inferred that reactions (7–10) are feasible at temperatures $\geq$ 1220, 1510, 1580 and 1540 °C, respectively under pressure of 1 atm. A similar inference has been also drawn by Zhang et al. [24], who have also shown that these

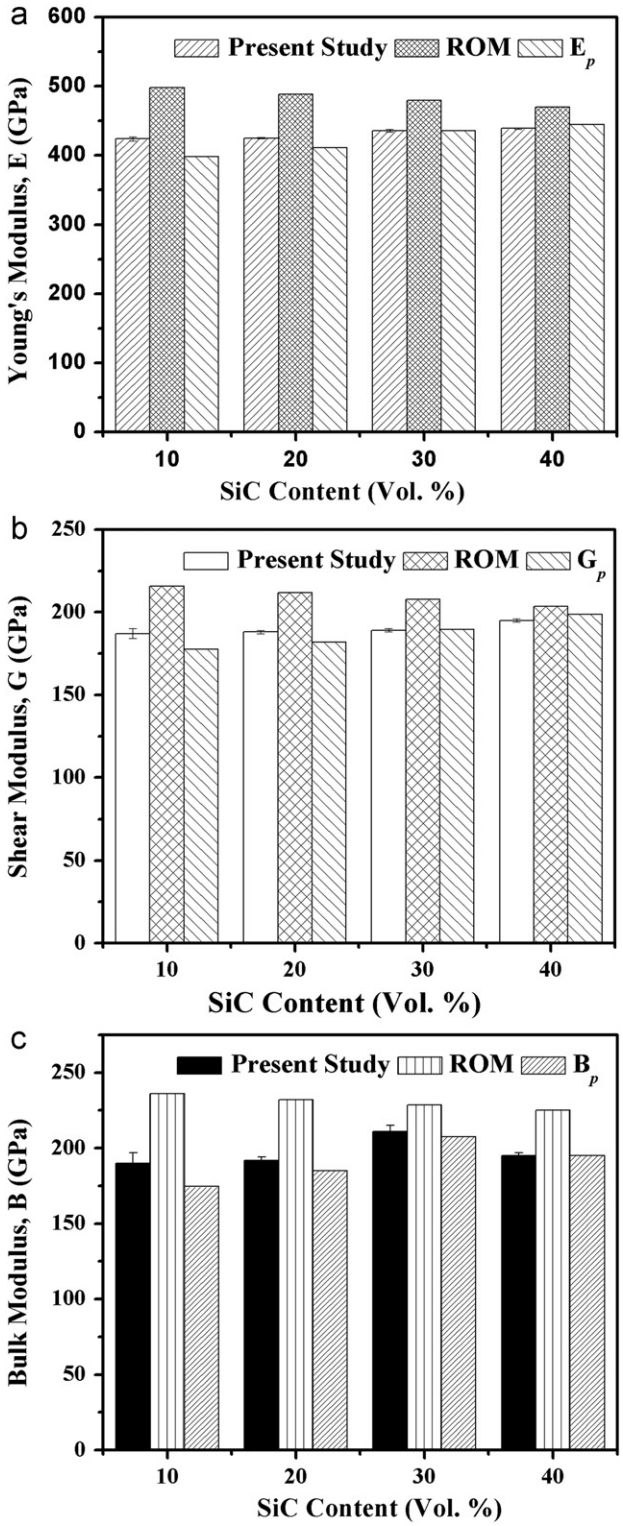

Fig. 15. Bar-charts depicting: (a) Young's modulus, (b) shear modulus, and (c) bulk modulus of the investigated composites along with values expected from ROM. The values of elastic modulus calculated using Eq. (12) are also shown for comparison.

reactions are likely to occur at much lower temperature in vacuum. From the above-mentioned analyses, it is inferred that both B_4C and C added to the raw materials as

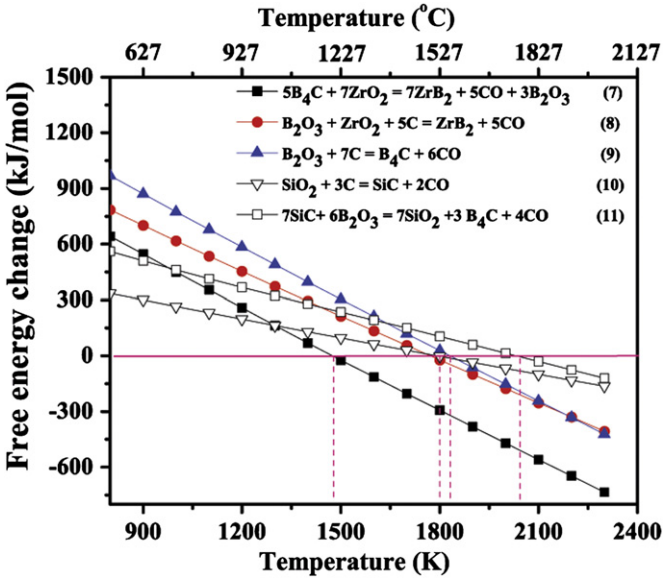

Fig. 16. Plots of free energy change against absolute temperature using thermodynamic data [39] for reactants and products.

sintering additives play a significant role in densification during presintering at intermediate temperatures in course of pressure-less sintering of the investigated composites by removal of the surface oxides (ZrO_2, SiO_2 and B_2O_3) from the powder particles of raw materials through reactions (7–10).

Through analysis of thermodynamic data, it is observed that reaction (11) is feasible at temperatures $\geq 1775\ ^\circ C$. This suggests that the SiC particles present as reinforcement or those formed by reaction (10) contribute to the process of densification at the sintering temperature by removal of B_2O_3. It is intuitive that increase in SiC volume fraction increases the net ZrB_2–SiC interfacial area, which in turn promotes reaction (11) at the sintering temperature causing the removal of B_2O_3, and thereby leads to densification.

4.1.3. Effect of impurities from milling media on reduction of oxides and densification

One of the possible chemical reactions leading to reduction of ZrO_2 by the WC, which is the impurity introduced in course of ball-milling is shown as follows [19]:

$$ZrO_2\ (s) + 3WC\ (s) \rightarrow 3W\ (s) + ZrC\ (s) + 2CO\ (g) \quad (12)$$

However, this reaction has been reported to be feasible only at temperatures $\geq 1960\ ^\circ C$ [19], based on thermodynamic analysis. Furthermore, it has been also shown that WC decomposes at temperatures $\geq 1500\ ^\circ C$ through the following reaction [19]:

$$WC \rightarrow W_2C + C \quad (13)$$

Then, reaction (13) is known to be followed by:

$$ZrO_2 + 3W_2C \rightarrow ZrC + 6W + 2CO \quad (14)$$

The possibilities of reactions ((12)–(14)) explain why the peaks of WC have not been found in the XRD patterns representing the sintered ZrB_2–SiC composites (Fig. 5). Moreover, examination of the isothermal section of the W–B–C ternary phase diagram indicates that WC and B_4C are not chemically compatible. Compatibility triangles in the isothermal section of the W–B–C ternary phase diagram indicate equilibrium phase fields comprising $W_2B_5+C+B_4C$, or $W+W_2C+W_2B$, or $WB+W_2B_5+C$ [40,41]. However, peaks of none of these phases could be observed in the XRD pattern from the sintered composite as shown in Fig. 5, indicating that the crystalline constituents of these phases are either not present or have insignificant volume fractions.

It may be noted that examination of SEM images and EDX maps has shown clear evidence for enrichment of W, Co and Fe at the ZrB_2 grain boundaries or ZrB_2–SiC interfaces (Fig. 9), where W appears to be contributed by reaction (14). Based on this assumption, it may be further proposed that the C-rich areas adjacent to the W-enriched locations at the ZrB_2–SiC interfaces, as shown in Fig. 9(a) could have formed during the decomposition of WC through reaction (13). Furthermore, through comparison of the XRD patterns obtained from pre-sintered and sintered ZSBC-30 composites, the ZrB_2 peak positions representing the latter material are found to be shifted marginally to the right. Moreover, the lattice constants (a and c) of ZrB_2 calculated using the Cohen's method [42] and shown in Table 3, are found to be lower for the matrix of sintered composite than those for the raw material. These observations along with the results of EDX analysis [Fig. 9(b)] showing the presence of C peak suggests that ZrC could have formed solid solution with ZrB_2, as has been proposed in earlier reports [19,22]. This possibility is supported by the fact that Zr–B–C ternary phase diagram [43] shows the solubility of ZrC in ZrB_2 to be 4.5 wt%. Furthermore, W is also reported to have limited amount of solubility in ZrB_2 [19,44]. The reduction in lattice constants may be attributed to smaller atomic radii of the substitutional solute atoms than that of parent lattice: $a_W(=1.38\ \text{Å}) < a_{Zr}(=1.57\ \text{Å})$; $a_C(=0.84\ \text{Å}) < a_B$ (0.93 Å) [19]. Thus, it is possible to explain why the peaks of both W and ZrC are not found in the XRD patterns obtained from the sintered composites. It should be also noted that the valencies of W and C are different from those of Zr and B. Therefore, the presence of C and W as substitutional solute in ZrB_2 is expected to cause the formation of charged point defects, which are expected to increase the solid-state diffusion rates [19], and thereby enhance the rate of densification.

Table 3
Lattice constants of ZrB_2 present in the ball-milled powder mixtures and sintered ZSBC-30.

ZrB_2 in	a (Å)	c (Å)
Ball-milled powder mixtures	3.1705	3.5302
Sintered ZSBC-30	3.1604	3.5218
% Decrease	0.32%	0.24%

Examination using EDX analysis on SEM has shown significant segregation of W, Fe, Co and C at some of the matrix grain boundaries and ZrB_2–SiC interfaces. Segregation of W at the matrix grain boundaries and particle–matrix interfaces may be considered to be helpful in the process of densification, as Kisley et al. [45] has shown that doping of ZrB_2 with W leads to increase in its surface diffusion. The peak of C in the EDX spectrum from the bright region at the ZrB_2 grain boundary [Fig. 9(b)] could be due to the presence of unreacted W_2C formed by reaction (13). As discussed above and also reported earlier [19], both W and C could be present as solute in ZrB_2. Therefore, it may be inferred that partitioning of W to ZrB_2 grain boundaries or ZrB_2–SiC interfaces in preference to forming solid solution with ZrB_2 could be probably promoted by local enrichment of Fe. Furthermore, analysis of ternary phase diagrams of W–Co–C [46,47] and W–Co–Fe systems [48] as well as W–Co–Fe–C quarternary systems [47], indicates that liquid phase could have formed at temperatures $< 2000\ ^\circ\text{C}$. Moreover, the continuity of the W-rich interfacial network along the ZrB_2 grain boundary as shown in Figs. 8 and 9 is suggestive of almost perfect wetting of the ZrB_2 grains by the liquid phase. In some of the earlier studies, liquid phase sintering has been found to lead to the formation of microfaceted grains or grains with rounded corners [49,50]. In this study too, the ZrB_2 grains surrounded by W and Fe-rich interfacial network appear to be faceted, as shown in Figs. 8, 9 and 12. Both interfacial segregation of Fe and its contribution to densification of ZrB_2 have been reported earlier by Mishra et al. [51,52] in a study involving self-propagating high temperature synthesis. It has been shown in an earlier study that Zr and B dissolve in liquid Fe and then crystallizes to form the $(Fe,Zr)_2B$ phase at the interfaces. Therefore, in the present study, based on the microstructural observations pertaining to the ZrB_2 grain boundaries, it is appropriate to infer that a limited amount of liquid phase is formed at a significant fraction of the matrix grain boundaries and ZrB_2–SiC interfaces during sintering of the investigated composites, and enhanced diffusion through this liquid could have contributed to the process of densification. The composites fabricated by pressureless sintering in this study have been found to retain their structural integrity in spite of their exposure to temperatures $\geq 2000\ ^\circ\text{C}$ at the tips of oxyacetylene flame [30], which suggests that these materials are stable at elevated temperatures in spite of impurity segregation at a fraction of the interfaces.

4.1.4. Role of SiC in grain growth inhibition

Grain growth is of interest in this study not only for its effect on mechanical properties, but also on densification. It is intuitive that increase in grain size leads to lowering of the driving force for densification. Earlier studies have shown that optimum densification can be achieved in ZrB_2

through inhibition of grain growth by reduction of surface oxides [22]. It may be noted that relative density obtained in the sample sintered at 2000 °C for 2 h is higher than that found on sintering for similar duration at 2050 °C. This observation may be attributed to significantly higher rate of grain coarsening than that of closure of porosities at the higher temperature.

The results in Fig. 10 indicate that the average matrix grain size of the investigated ZrB_2–SiC composite increases with increase in duration of sintering at 2000 °C. Furthermore, comparison of the linear regressional parameters pertaining to grain growth as shown in Table 3 leads to the following inferences: (i) there exists a linear relationship between average grain size and duration of sintering; (ii) the rate of grain growth with duration of sintering decreases with increasing SiC volume fraction; and (iii) the grain size at time (t)=0 increases with decrease in SiC content. Furthermore, qualitative examination of the matrix grains in Fig. 7(a) through (e), and the results depicted in Fig. 10 reveal that grain growth during sintering is inhibited by the presence of SiC particles as reinforcement. It is well-established that the fine SiC particles restrict grain growth by pinning of the ZrB_2 grain boundaries during sintering [24,37]. Moreover, removal of intergranular B_2O_3 by reaction with SiC (Reaction (11)) is also expected to restrict the grain growth. However, the average size and aspect ratios of the SiC particles have been found to increase with increase in its volume fraction. The increase in size is more drastic at volume fractions of 30 or 40, for which the SiC particles appear to form a more or less interconnected network.

Based on the estimated slopes (Table 2) of the best-fit lines for the plots in Fig. 10, it is proposed that different amounts of matrix grain growth occurs during heating of the samples to the temperature of sintering, depending on the SiC content of the investigated composites. Of course, it should be noted that the amount of grain growth observed during heating is much less significant compared to that during isothermal holding at elevated temperatures. Prevention of grain growth by the SiC particles is expected to have also contributed to the process of densification by promoting closure of the interparticle voids through intergranular and surface diffusion at relatively low temperatures. The growth in size and aspect ratios of SiC particles as observed in this study have been reported earlier as well [24,53], and may be attributed to their coalescence along the ZrB_2 grain boundaries [53]. A near-continuous network of SiC particles is expected to inhibit grain coarsening by effectively increasing the diffusion distances between neighboring ZrB_2 grains.

4.2. Microstructure–mechanical property relationship

4.2.1. Microhardness

The microhardness of the investigated composites has been found to depend on their SiC content as well as temperature and duration of sintering, as is obvious from the results depicted in Fig. 13. The average microhardness of the composites sintered for 2 h increases by 30.4%, as their SiC content is increased from 10 to 40 vol%, which is attributed to the combined effect of higher hardness of SiC than that of the ZrB_2 matrix, as well as decrease in ZrB_2 grain size and increased densification with increasing SiC content. The increase in ZrB_2 grain size is also expected to cause increase in the amount of microcracking due to internal residual stresses generated during cooling from the processing temperature because of thermal expansion anisotropy between different crystallographic directions. With decrease in the ZrB_2 grain size and increase in the amount of densification, the possibility of microcrack formation in the matrix during cooling is expected to be minimized, which is believed to be responsible for rise in the matrix microhardness. The results of earlier studies [54,55] have shown that the increase in grain size by $\sim$1.2 to $\sim$2.5 times that of the initial ZrB_2 particle size have relatively insignificant effect on hardness of the ZrB_2–SiC composites. However, as the observed increase in the matrix grain size during sintering in the present study is $\approx$2–3 times more than that reported by Rezaie et al. [54] and Guo et al. [55], its influence on microhardness is also found to be more significant.

In tune with the above discussion, the decrease in microhardness on sintering at 2000 °C for durations beyond $\approx$2 h (as shown in Fig. 13) can be attributed to the increase in the average matrix grain size, as shown in Fig. 10. Similar explanation can also be proposed for lower microhardness observed for the composite samples sintered at 1950 and 2050 °C, which have lower relative density and larger average matrix grain size, respectively than the values recorded for the composite sintered at 2000 °C.

4.2.2. Indentation fracture behavior

As shown in Fig. 14(a), the IFT of the investigated composites is increased by $\approx$26.7% with increase in the SiC content from 10 to 40 vol%. Although the values of IFT are known to possess higher degree of uncertainty compared to those obtained from conventional fracture toughness tests, these data can be used effectively to compare the toughness of the small volume specimens, and examine the mechanisms of crack-particle interactions. The interaction of indentation cracks with the SiC particles as shown in Fig. 14(b), leads to crack deflection, and branching, which in turn are known to cause toughening of the investigated composites. Similar observation of crack-particle interaction has also been reported for the ZrB_2–SiC composite by Zhang et al. [24]. The increase in the value of IFT with increase in SiC volume fraction can be attributed to increase in both frequency of crack-particle interaction and SiC aspect ratio with increase in SiC volume fraction. These results follow the pattern of experimental results reported for different types of ceramic–ceramic composites [56,57]. Theoretical predictions by Faber and Evans [58] indicate a larger amount

of crack deflection and therefore greater degree of toughening for reinforcements with higher aspect ratios. The decrease in matrix grain size of the investigated composites with increase in the SiC volume fraction could also be partly responsible for the observed increase in IFT, because of the reduction in the amount of damage caused by thermal residual stresses as discussed above (Section 4.2.1).

4.2.3. Elastic modulus

Comparison of the results shown in Fig. 15 indicate that (i) the experimentally obtained values of E, G and B are lower by 7–15%, 4–13% and 8–20%, respectively than those of their corresponding ROM values and (ii) deviations of the experimentally obtained values from those expected from ROM are relatively lower for the composites with higher SiC content. Considering that the relative densities of the composites scale with their SiC volume fractions, the differences in the values of elastic properties with the ROM values are attributed to the presence of porosity in their microstructures. The relationship between the amount of porosity and Young's modulus proposed by Nielsen [59] is:

$$E_p = \frac{E_0(1-P)^2}{1+(1/N_s-1)P} \quad (14)$$

where E_p is the Young's modulus of specimens with pore volume fraction P, E_0 is the Young's modulus without any porosity ($\approx$ the value predicted by ROM), and N_s is the Neilsen shape factor (0.4). The values of E_p calculated using Eq. (14) for the investigated composites are also shown in Fig. 15(a). Moreover, using the values of E_p and υ, the values of shear modulus (G_p) and bulk modulus (B_p) have been calculated, and are shown in Fig. 15(b) and (c), respectively. On examination of the results in Fig. 15, it is also found that the agreement between E_p and the experimentally obtained values is excellent for the composites with higher SiC contents, which usually possess higher relative densities. The maximum difference of $\approx 6.1\%$ is found between E_p and experimentally obtained Young's modulus for the ZSBC-10 composite, which exhibits the highest porosity content ($\approx 6.7\%$) among the investigated composites.

4.3. Comparisons with earlier studies

It may be noted that the experimental procedure of the present study differs from that followed in different previous investigations involving pressureless sintering [19–29] in not having the cold isostatic pressing step, compositions of raw materials (oxygen content and types or amounts of sintering additives), as well as choice of the combination of temperatures and durations of both sintering and intermediate hold. In majority of the earlier studies [20,22,24] involving pressureless sintering, the uniaxially pressed pellets were subjected to the additional consolidation step of cold isostatic pressing under an applied pressure of 250 or 300 MPa. It is well-known that cold isostatic pressing of the pellets could lead to more uniform density distribution within the green compact than that possible by uniaxial pressing. In spite of only uniaxial compaction used to consolidate the powders, the relative densities of the compacts are found to be more or less comparable to those reported earlier in the literature, probably because the heights of the pellets taken in this study were quite small. Moreover, use of SiC with particle size finer than that of ZrB_2 and addition of WC as impurity during ball-milling also appear to have contributed to the process of densification.

It may be noted that majority of the earlier studies [19–23] have focused on pressureless sintering of either monolithic ZrB_2 or ZrB_2–SiC composites with selected volume fractions of SiC, whereas the present study has primarily emphasized on the role of SiC particles along with those of additives and impurities. The report by Zhang et al. [24] shows increase in the amount of densification with increasing SiC content for certain selections of raw materials and sintering temperature, whereas no definite trend could be observed for certain other cases. However, in the present study, the amount of densification is found to increase consistently with increasing SiC content for all durations of sintering with or without holding at intermediate temperatures. Of course, the presence of SiC has been found to inhibit grain growth in ZrB_2 in this study, which is consistent with that reported earlier [24,37].

The differences between the types of results found for this study and that by Zhang et al. [24] could be attributed to differences in the average sizes of raw material powders, oxygen content, and the amount of impurities added during ball milling. The average oxygen content of the constituents of raw materials used in the present study is less than that by Zhang et al. [24] by $\approx 10\%$. But, the amount of C added as phenolic resin in this study is less by $\approx 57\%$ compared to the minimum amount (i.e., $\approx 2.8\%$) present in the raw materials used by Zhang et al., whereas it is more or less as similar to that used by Zhu et al. [21] for sintering of monolithic ZrB_2. Based on these comparisons, it appears that the amount of C obtained from the phenolic resin used in this study was insufficient to reduce the oxide impurities completely. However, in spite of insufficient C addition, the maximum relative densities obtained for the investigated ZrB_2–SiC composites are high and comparable to those achieved by other investigators [24,60,61]. Hence, reactions (11)–(14) involving SiC and WC phases have a very critical role in reduction of residual oxides, which in turn promotes densification. This inference is further supported by the fact that the amount of densification (relative density of $\approx 83\%$) observed in case of monolithic ZrB_2 in this study has been found to be much poorer than that found for any of the ZrB_2–SiC composites. It is also appropriate to infer that the positive role of SiC in the process of densification is particularly noticed, if the C content of the raw materials is insufficient in comparison to the net oxygen content.

The average matrix grain size observed in the ZrB_2–SiC composites obtained by pressureless sintering in this study has been found to be $\approx$2–4 times more than that reported by

Zhang et al. [24] for the composites with identical SiC volume fractions. The results of thermodynamic analyses as discussed in Section 3.2 indicate that reactions involving reduction of the impurity oxides by C occur for the experiments carried out at atmospheric pressure (as expected for experiments carried out in flowing argon) in the range of 1510–1580 °C, whereas further reduction of B_2O_3 by SiC occurs at 1850 °C. However, in the study by Zhang et al., the ZrB_2 or SiC grain growth could be effectively restricted by reduction of B_2O_3 by reaction with C in vacuum at a significantly lower temperature of ≈1000 °C, which in turn has prevented the formation of borosilicate glass at matrix grain boundaries or particle–matrix interfaces.

Comparison of the present results of ZSBC-20 with those obtained for the ZrB_2-20 SiC composites processed by pressureless sintering using either B [60] or Mo [31] indicates that the relative densities and hardness are more or less comparable for all these materials. However, the Young's modulus of ZSBC-20 is found to be higher than that obtained by Zhang et al. [61] for the ZrB_2-20 SiC composite prepared by pressureless sintering at 2100 °C using B_4C and phenolic resin as additives, which could be due to the differences in test procedures.

The relative density, Young's modulus, Poisson's ratio, hardness and IFT of ZrB_2-20 vol% SiC composite prepared by hot pressing at 2000 °C using the same raw materials as in the present study, have been reported as 99.8%, 484 GPa, 0.13, 19.4 GPa and 6.7 $MPa\sqrt{m}$, respectively [62]. Except for Poisson's ratio and IFT, the highest values of both Young's modulus and hardness are found to be lower by ≈6–7% for the composites prepared by pressureless sintering technique. Lower Young's modulus of the composite prepared by pressureless sintering compared to those found for the corresponding hot-pressed product is attributed to slightly lower relative density, coarser matrix grain size and grain boundary segregation of impurities (W, Co and Fe) in the former material. On the other hand, lower hardness of the pressureless sintered sample could be due to its grain size being coarser than that of the hot pressed samples, in addition to the factors responsible for lower Young's modulus as mentioned above. The above comparative assessment indicates that pressureless sintering process needs to be further refined to obtain desirable grain size and mechanical properties comparable to those of the hot pressed composites. Still, for fabrication of ZrB_2–SiC composites based components, the method of pressureless sintering as attempted in this study may be preferred because it is relatively inexpensive compared to hot pressing, or other alternative processes involving cold isostatic pressing. Moreover, for processing of components with complex shapes, pressureless sintering can be considered as more appropriate than hot pressing.

5. Conclusions

The following conclusions can be drawn based on the studies related to pessureless sintering of ZrB_2–SiC composites with B_4C and C (added as phenolic resin) as additives:

(1). The use of B_4C and C as sintering additives as well as presence of impurities such as W, Co and Fe promote densification by reduction of the oxide impurities comprising ZrO_2 and SiO_2 in the powder mixture used as raw material.
(2). Sintering at 2000 °C has been found to lead to higher relative density than that at either 1950 or 2050 °C. Relatively lower rate of mass transport at 1950 °C, and higher rate of grain growth at 2050 °C appear to limit the amount of densification at these temperatures.
(3). Relative densities of both green compacts and sintered products are found to increase with increase in the volume fraction of SiC particles. The increase in green density with amount of SiC may be attributed to its particle size being finer than that of ZrB_2. The presence of SiC is also beneficial for densification during sintering, because it participates in reducing B_2O_3 at the ZrB_2–SiC interfaces, restricts grain growth.
(4). The amount of WC in the ball-milled powder mixtures has been found to increase with the SiC content of the composites. During sintering, decomposition of WC and its role in reducing ZrO_2 is found to promote densification. Segregation of W, Co and Fe has been found at the ZrB_2 grain boundaries or ZrB_2–SiC interfaces. Formation of liquid phase at such interfaces appears to aide in the process of densification.
(5). Microhardness of the composites is found to increase with duration of sintering up to 1 or 2 h depending on their composition due to increase in relative density of the investigated composites. With further increase in the time of sintering, hardness is found to decrease due to grain growth.
(6). Values of elastic modulus of the composites are found to be closer to those predicted by the rule of mixtures only for the composites with higher SiC content. This observation has been attributed to lowering of elastic modulus with increased porosity, and this phenomenon can be predicted using Nielsen's relationship.

Acknowledgements

The financial support received from Defence Research and Development Organization for carrying out research and that from Central Scientific and Industrial Research, New Delhi as stipend for one of the authors (M. Mallik) are gratefully acknowledged. The authors also express their sincere gratitude to Mr. Rajiv Khalko, staff member at Powder Metallurgy Laboratory of the Department, Mr. Tapas Paul, Mr. Ranadhir Bosu, Mr. Sukanta Mondal, Mr. Mithun Das, and Mr. M.B. Pusty, staff members at the Central Research Facility, Indian Institute of Technology,

Kharagpur, West Bengal, India for technical assistance in carrying out this work.

References

[1] W.G. Fahrenholtz, G.E. Hilmas, I.G. Talmy, J.A. Zaykoski, Refractory diborides of zirconium and hafnium, Journal of the American Ceramic Society 90 (2007) 1347–1364.

[2] K. Upadhya, J.M. Yang, W.P. Hoffmann, Materials for ultrahigh temperature structural applications, American Ceramic Society Bulletin 76 (1997) 51–56.

[3] M.J. Gasch, D.T. Ellerby, S.M. Johnson, Ultra-high temperature ceramic composites, in: N.P. Bansal (Ed.), Handbook of Ceramic Composites, Kluwer Academic Publishers, Boston, 2005, pp. 197–224.

[4] R.A. Cutler, Engineering properties of borides, in: S.J. Schneider (Ed.), Ceramics and Glasses, Engineered Materials Handbook, Vol. 4, ASM International, Materials Park, OH, 1992, pp. 787–803.

[5] S.R. Levine, E.J. Opila, M.C. Halbig, J.D. Kiser, M. Singh, J.A. Salem, Evaluation of ultra high temperature ceramics for aeropropulsion use, Journal of the European Ceramic Society 22 (2002) 2757–2767.

[6] A.S. Brown, Hypersonic designs with a sharp edge, Aero. Am 35 (1997) 20–21.

[7] K. Kuwabara, Some characteristics and applications of ZrB_2 ceramics, Bulletin of the Ceramic Society of Japan 37 (2002) 267–271.

[8] S. Norasetthekul, P.T. Eubank, W.L. Bradley, B. Bozkurt, B. Stucker, Use of Zirconium diboride-copper as an electrode in plasma applications, Journal of Materials Science 34 (1999) 1261–1270.

[9] M. Pastor, Metallic borides: preparation of solid bodies, sintering methods and properties of solid bodies, in: V.I. Matkovich (Ed.), Boron and Refractory Borides, Springer, New York, 1977, pp. 457–493.

[10] G.A. Meeson, A.F. Gorbunow, Activated sintering of zirconium boride,, Inorganic Materials 4 (1968) 267–270.

[11] M. Kinoshita, S. Kose, Y. Hamano, Hot-pressing of zirconium diboride-molybdenum disilicide mixtures, Yogyo-Kyokai-Shi 78 (1970) 32–41.

[12] S.Q. Guo, J.M. Yang, H. Tanaka, Y. Kagawa, Effect of thermal exposure on strength of ZrB_2-based composites with nano-sized SiC particles, Composites Science and Technology 68 (2008) 3033–3040.

[13] D. Kalish, E.V. Clougherty, Densification mechanisms in high-pressure hot-pressing of HfB_2, Journal of the American Ceramic Society 52 (1969) 26–30.

[14] D. Kalish, E.V. Clougherty, K. Kreder, Strength, fracture mode, and thermal stress resistance of HfB_2 and ZrB_2, Journal of the American Ceramic Society 52 (1969) 30–36.

[15] O. Kida, Y. Segawa, ZrB_2 Composite Sintered Material, U.S. Patent 4,636,481, January 13, 1987.

[16] O. Kida, Y. Segawa, ZrB_2 Composite Sintered Material, U.S. Patent 4,668,643, May 26, 1987.

[17] L. Silvestroni, D. Sciti, Effects of $MoSi_2$ additions on the properties of Hf–and Zr–B_2 composites produced by pressureless sintering, Scripta Materialia 57 (2007) 165–168.

[18] D. Sciti, S. Guicciardi, A. Bellosi, G. Pezzotti, Properties of a pressureless-sintered ZrB_2–$MoSi_2$ ceramic composite, Journal of the American Ceramic Society 89 (2006) 2320–2322.

[19] A.L. Chamberlain, W.G. Fahrenholtz, G.E. Hilmas, Pressureless sintering of zirconium diboride, Journal of the American Ceramic Society 89 (2006) 450–456.

[20] S.C. Zhang, G.E. Hilmas, W.G. Fahrenholtz, Pressureless densification of zirconium diboride with boron carbide additives, Journal of the American Ceramic Society 89 (2006) 1544–1550.

[21] S. Zhu, W.G. Fahrenholtz, G.E. Hilmas, S.C. Zhang, Pressureless sintering of zirconium diboride using boron carbide and carbon additions, Journal of the American Ceramic Society 90 (2007) 3660–3663.

[22] S. Zhu, W.G. Fahrenholtz, G.E. Hilmas, S.C. Zhang, Pressureless sintering of carbon-coated zirconium diboride powders, Materials Science and Engineering A 459 (2007) 167–171.

[23] W.G. Fahrenholtz, G.E. Hilmas, S.C. Zhang, S. Zhu, Pressureless sintering of zirconium diboride: particle size and additive effects, Journal of the American Ceramic Society 91 (2008) 1398–1404.

[24] S. Zhang, G.E. Hilmas, W.G. Fahrenholtz, Pressureless sintering of ZrB_2–SiC ceramics, Journal of the American Ceramic Society 91 (2008) 26–32.

[25] S.Q. Guo, Densification of ZrB_2-based and their mechanical and physical properties: A review, Journal of the European Ceramic Society 29 (2009) 995–1011.

[26] Guo-Jun Ji Zou, Yan-Mei Zhang, Kan, Pei-Ling Wang, Pressureless densification of ZrB_2–SiC composites with vanadium carbide, Scripta Materialia 59 (2008) 309–312.

[27] Guo-Jun Ji Zou, Zhang, Yan-Mei Kan, Formation of tough interlocking microstructure in ZrB_2–SiC-based ultrahigh-temperature ceramics by pressureless sintering, Journal of Materials Research 24 (7) (2009) 2428–2434.

[28] Shi C. Zhang, Greg E. Hilmas, William G. Fahrenholz, Improved oxidation resistance of zirconium diboride by tungsten carbide additions,, Journal of the American Ceramic Society 91 (11) (2008) 3530–3535.

[29] Youngjie Hui Zhang, Zhengren Yan, Xuejian Huang, Liu, Dongliang Jiang, Pressureless sintering of ZrB_2–SiC ceramics: the effect of B_4C content, Scripta Materialia 60 (2009) 559–562.

[30] M. Mallik, R. Mitra, K.K. Ray, Processing and properties of advanced ceramics and composites II, in: N.P. Bansal, J.P. Singh, J. Lamon, S.R. Choi, M.M. Mahmoud (Eds.), Ceramic Transactions, Wiley, Hoboken, NJ, 2010, pp. 77–90.

[31] K. Nihara, R. Morena, D.P.H. Hasselman, Indentation fracture toughness of brittle materials for Palmqvist cracks, in: R.C. Bradt, D.P.H. Hasselman, F.F. Lange (Eds.), Brittle Matrix Composites 2, Elsevier Applied Science, New York, 1983, pp. 84–97.

[32] Y. Yan, Z. Huang, S. Dong, D. Jiang, Pressureless sintering of high density ZrB_2–SiC ceramic composites, Journal of the American Ceramic Society 89 (2006) 3589–3592.

[33] Z. Cheng, C. Zhou, T. Tian, C. Sun, Z. Shi, J. Fan, Pressureless sintering of ultra-high temperature ZrB_2–SiC Ceramics, Key Engineering Materials 368–372 (2008) 1746–1749.

[34] D.E. Wiley, W.R. Manning, O. Hunter JR, Elastic properties of polycrystalline TiB_2, ZrB_2 and HfB_2 from room temperature 1300 K, Journal of Less-Common Metals 18 (1969) 149–157.

[35] R.G. Munro, Material properties of a sintered alpha-SiC, Journal of Physical and Chemical Reference Data (1997) 1195–1203.

[36] E.J. Edrees, A.C. Smith, A. Hendry, A rule of mixtures model for sintering of particle-reinforced ceramic matrix composites, Journal of the European Ceramic Society 18 (1998) 275–278.

[37] S.M. Zhu, W.G. Fahrenholtz, G.E. Hilmas, Influence of silicon carbide particle size on the microstructure and mechanical properties of zirconium diboride-silicon carbide ceramics,, Journal of the European Ceramic Society 27 (2007) 2077–2083.

[38] B_2O_3–SiO_2 phase diagram, Fig. 9273, phase equilibria diagrams, vol. XI, Robert S. Roth (Eds.), American Ceramic Society Inc., (1995) p. 112.

[39] M.W.Chase.Jr., TNIST-JANAF hermochemical Tables, Journal of Physical and Chemical Reference Data, 736 Monograph 9, fourth ed.Woodbury, NY: American Institute for Physics; 1998.

[40] ACerS-NIST, ACerS-NIST Phase Equilibria Diagrams, CD-ROM Database, Ver. 3.0.1. Fig. 08873, The American Ceramic Society, Westerville, OH.

[41] Harlan J. Brown-Shaklee, William J. Fahrenholtz, Greg E. Hilmas, Densification behavior and microstructural evolution of hot-pressed HfB_2, Journal of the American Ceramic Society 94 (1) (2011) 49–58.

[42] B.D. Cullity, Elements of X-ray Diffraction, Second ed., Addison-Wesley Publishing Company, Inc., 1978, p. 363.

[43] A.E. McHale (Ed.), Figure 8874 in Phase Equilibria Diagrams—Phase Diagrams for Ceramists, X, Borides, Carbides and Nitrides, The American Ceramic Society, Westerville, OH, 1994.
[44] A.E. McHale (Ed.), Figure 8851 in Phase Equilibria Diagrams—Phase Diagrams for Ceramists, Vol. X, Borides, Carbides and Nitrides, The American Ceramic Society, Westerville, OH, 1994.
[45] P.S. Kisliy, M.A. Kuzenkova, O.V. Zaveruha, On the sintering process of zirconium diboride with tungsten, Physics of Sintering 3 (1) (1971) 31–43.
[46] A. Markstrom, B. Sundman, K. Frisk, A revised thermodynamic description of the Co–W–C system, Journal of Phase Equilibrium and Diffusion 26 (2) (2005) 152–160.
[47] V. Raghavan, Carbon–Cobalt–Iron–Nickel–Tungsten, Journal of Phase Equilibrium and Diffusion 28 (3) (2007) 284–285.
[48] Lesley Cornish, Andy Watson, Cobalt–Iron–Tungsten, In Iron Systems: Phase Diagrams, Crystallographic and Thermodynamic Data, vol. 11D3: Iron Systems, Part 3, Günter Effenberg, Svitlana Ilyenko (Eds.), Chap. DOI 10.1007/978-3-540-74199-2_5, Book DOI 10.1007/978-3-540-74199-2.
[49] Randall M. German, Pavan Suri, and Siong Jin Park, Review: liquid phase sintering. Journal of Materials Science 44 (199) 1-68.
[50] Neha Gupta, Amartya Mukhopadhyay, K. Pavani, Bikramjit Basu, Spark plasma sintering of novel ZrB2–SiC–TiSi2 composites with better mechanical properties, Materials Science and Engineering A 534 (2012) 111–118.
[51] S.K. Mishra (Pathak), S. Das, S.K. Das, P. Ramachandra Rao, Sintering studies on ultrafine ZrB_2 powder produced by a self-propagating high-temperature synthesis process, Journal of Materials Research 15 (11) (2000) 2499–2504.
[52] S.K. Mishra, S. Das, P. Ramachandra Rao, Microstructure evolution during sintering of self-propagating high-temperature synthesis produced ZrB_2 powder, Journal of Materials Research 17 (11) (2002) 2809–2814.
[53] D. Sciti, L. Silvestroni, V. Medri, S. Guicciardi, Pressureless sintered in-situ toughened ZrB_2–SiC platelet ceramics, Journal of the European Ceramic Society 31 (2011) 2145–2153.
[54] A. Rezaie, W.G. Fahrenholtz, G.E. Hilmas, Effect of hot pressing time and temperature on the microstructure and mechanical properties of ZrB_2–SiC, Journal of Materials Science 42 (2007) 2735–2744.
[55] W.M. Guo, G.J. Zhang, P.L Wang, Microstructural evolution and grain growth kinetics in ZrB_2–SiC composites during heat treatment, Journal of the American Ceramic Society 92 (2009) 2780–2783.
[56] A.K. Bhattacharya, J.J. Petrovic, Hardness and fracture-toughness of SiC particle reinforced $MoSi_2$ composites, Journal of the American Ceramic Society 74 (1991) 2700–2703.
[57] K.T. Faber, A.G. Evans, Crack deflection processes-II, Experiment, Acta Metall 31 (1983) 577–584.
[58] K.T. Faber, A.G. Evans, Crack deflection processes-I. Theory, Acta Metallurgica 31 (1983) 565–576.
[59] L.F. Nielsen, Elasticity and damping of porous materials and impregnated materials, Journal of the American Ceramic Society 67 (1984) 93–98.
[60] X.G. Wang, W.M. Guo, G.J. Zhang, Pressureless sintering mechanism and microstructure of ZrB_2–SiC ceramics doped with boron, Scripta Materialia 61 (2009) 177–180.
[61] H. Zhang, Y. Yan, Z. Huang, X. Liu, D. Jiang, Properties of ZrB_2–SiC ceramics by pressureless sintering, Journal of the American Ceramic Society 92 (2009) 1599–1602.
[62] R. Mitra, S. Upender, M. Mallik, S. Chakraborty, K.K. Ray, Mechanical, thermal and oxidation behavior of zirconium diboride based ultra-high temperature ceramic composites, Key Engineering Materials 395 (2009) 55–68.